Hidden symmetries generate rigid folding mechanisms in periodic origami

James McInerney[a], **Bryan Gin-ge Chen**[e], **Louis Theran**[c], **Christian Santangelo**[b,d], **and Zeb Rocklin**[a]

[a]School of Physics, Georgia Institute of Technology, Atlanta, GA 30332; [b]Department of Physics, University of Massachusetts Amherst, Amherst, Massachusetts 01003; [c]School of Mathematics and Statistics, University of St Andrews, St Andrews, Scotland; [d]Department of Physics, Syracuse University, Syracuse, NY, 13244; [e]Department of Physics and Astronomy, University of Pennsylvania, Philadelphia, PA, 19104

This manuscript was compiled on September 10, 2020

We consider the zero-energy deformations of periodic origami sheets with generic crease patterns. Using a mapping from the linear folding motions of such sheets to force-bearing modes in conjunction with the Maxwell-Calladine index theorem we derive a relation between the number of linear folding motions and the number of rigid body modes that depends only on the average coordination number of the origami's vertices. This supports the recent result by Tachi which shows periodic origami sheets with triangular faces exhibit two-dimensional spaces of rigidly foldable cylindrical configurations. We also find, through analytical calculation and numerical simulation, branching of this configuration space from the flat state due to geometric compatibility constraints that prohibit finite Gaussian curvature. The same counting argument leads to pairing of spatially varying modes at opposite wavenumber in triangulated origami, preventing topological polarization but permitting a family of zero energy deformations in the bulk that may be used to reconfigure the origami sheet.

origami | mechanisms | rigid folding | topological polarization

1. Introduction

Origami-inspired materials are thin sheets whose two-dimensional crease patterns control their three-dimensional mechanical response, now manufacturable at the macroscopic scale using shape-memory alloys (1, 2) and the microscopic scale using graphene bilayers (3) or polymer films (4–6). Origami principles are used to engineer deployable solar cells (7), stent grafts (8), flexible electronics (9, 10), impact mitigation devices (11), and tunable antennas (12) as well as characterize patterns in biological systems (13). Yet determining whether a crease pattern can be rigidly folded into a particular shape is an NP-hard problem (14) due to nonlinear geometric constraints (15) that can lead to disjoint (16) or branched (17–20) configuration spaces with multiple energetic minima (21, 22).

Periodic origami sheets yield uniform mechanical properties such as negative Poisson ratios (23–27) and high stiffness-to-weight ratios (28), making them apt for the design of mechanical metamaterials. However, the study of origami tessellations has typically focused on crease patterns with inherent symmetries, such as the parallelogram faces of the Miura-ori (23, 24), which both simplify their analysis and generate rigid folding motions (29–31) that would cost energy in the absence of these symmetries (32). One might naively expect such symmetries are required as triangulations of all convex polyhedra are rigid (33). However, Tachi recently found origami sheets composed of repeating unit cells with triangular but otherwise generic faces rigidly fold between cylindrical configurations, indicating that crease topology (the number of edges and vertices) may play as important a role as crease geometry (the angles between these edges) in determining origami kinematics (34).

In the present work, we similarly consider generic triangulations, which inform the general case in three vital ways. First, the rigidly foldable configurations of *any* origami sheet can be derived as a subset of its triangulation's configurations. Second, the *low-energy* deformations of origami sheets are often well-approximated by the *rigid* configurations of their triangulations (35, 36). Finally, the triangulations are at the "Maxwell point": they have an equal number of constraints and degrees of freedom (37, 38), which we emphasize by calling them *Maxwell origami*. Mechanical systems at the Maxwell point generically possess large numbers of both zero energy modes and force-bearing modes (39, 40) which can be localized to the boundary via topological polarization (37, 38, 41), provide directional response in the bulk (42, 43), and tuned by reconfigurations of the network (44). However, origami sheets possess a geometrical duality between these two classes of modes (33, 45, 46) that, as we show, both permits the rigid foldability (34) and modifies its topological class, prohibiting the topological polarization (47) of Maxwell origami which limits the ability to engineer directional response.

The remainder of the paper is organized as follows. First, we review the work of Tachi to show Maxwell origami generically approximates a cylindrical sheet with two degrees of freedom (34). Next, we construct an index theorem that pairs folding motions with continuous symmetries in Maxwell

Significance Statement

The traditional approach to designing origami metamaterials uses particular, highly symmetric crease patterns to generate folding motions for reconfigurability. We instead consider origami sheets with periodic but otherwise generic, asymmetric triangular faces and show they exhibit nonlinear folding motions which transform sheets through two-dimensional families of cylindrical configurations, with the addition of quadrilateral faces restricting sheets to one-dimensional subsets of configurations. This leads to a novel topological class of mechanical modes, preventing origami from exhibiting exponentially localized floppy modes observed in other systems. These results do not depend on scale or material and hence have applications extending to architecture and robotics, but particularly to the nanoscale, where limited control over fold patterns can constrain traditional techniques.

All authors designed and performed research. J.M. and D.Z.R. wrote the manuscript.

The authors declare no conflicts of interest.

[2]To whom correspondence should be addressed. E-mail: zebrocklingatech.edu

origami. We then show the restriction to cylindrical configurations leads to distinct branches of nonlinearly foldable origami configurations that we confirm through numerical simulation. Finally, we extend our index theorem to accommodate spatially varying modes to explain the observed lack of topological polarization in Maxwell origami (47), and report lines of bulk modes with real wavenumber.

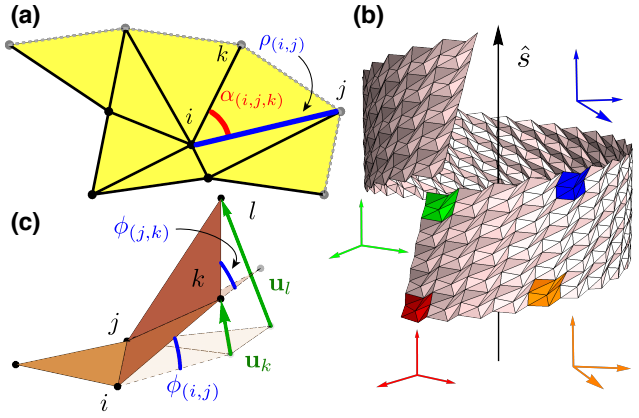

Fig. 1. (a) An origami unit cell with vertices labeled by Roman indices, sector angles labeled by $\alpha_{(i,j,k)}$, and fold angles labeled by $\rho_{(i,k)}$. (b) A generic, periodic origami sheet with cylindrical symmetries that follow from vertex compatibility with the unit cell highlighted in yellow. The screw periodicity of these sheets implies an orthonormal frame rotates between cells by the cell rotation matrices $\mathbf{S}_{1(2)}$. (c) The zero modes of an origami sheet can be specified either by the vertex displacements, $\mathbf{u}_i$, on every vertex i or the changes in folding angles, $\phi_{(i,j)}$ on every edge (i,j). The vertex displacements due to a folding motion accumulate allowing for non-zero curvature.

2. Cylindrical symmetries as a consequence of periodic origami angles

Origami sheets are parameterized by fixed patterns of straight creases along which they can be folded rigidly, in the sense that no face bends or stretches. This rigidity constraint determines what folded configurations are compatible with the underlying crease pattern. Here, we introduce our notation and describe the most general origami structures with periodic folds, as previously explored by Tachi (34).

We consider origami composed of unit cells, as depicted in Fig. 1a, with sector angles $\alpha_{(i,j,k)}$ subtended by vertex-sharing edges $\mathbf{r}_{(i,j)}$ and $\mathbf{r}_{(i,k)}$, and fold angles $\rho_{(i,j)}$, given by the supplement of the respective dihedral angles, between pairs of adjacent faces (defined such that $\rho_{(i,j)} = 0$ in a flat sheet), are identical in every cell, which are themselves indexed by $\mathbf{n} = (n_1, n_2)$. We do not require that the origami be developable, so that the sector angles need not sum to 2π around a vertex.

A necessary and sufficient condition for a set of fold angles to comprise a valid rigid fold about a vertex is for the successive rotations induced by traveling about the vertex to yield the identity rotation. This leads to the vertex condition derived in SI Appendix 1 (15)

$$\mathbf{F}_i = \prod_{(i,j)} \mathbf{R}_z(\alpha_{(i,j,k)})\mathbf{R}_x(\rho_{(i,j)}) = \mathbf{I}, \qquad [1]$$

where j,k takes on the successive indices of vertices connected to vertex i in counter-clockwise order and $\mathbf{R}_x, \mathbf{R}_z$ are matrices representing rotations about the x- and z-axes. For a simply connected sheet (as opposed to kirigami sheets with holes), this condition imposed at each vertex is sufficient to ensure rigid folding of the entire sheet.

Furthermore, the periodicity of sector angles between cells ensures that periodic fold angles can satisfy this condition in every cell. However, such periodic angles do not ensure that adjacent cells will have the identical orientations of normal crystalline structures. Instead, lattice rotation matrices

$$\mathbf{S}_{1(2)} \equiv \prod_{1(2)} \mathbf{R}(\rho_{(i,j)}, \hat{r}_{(i,j)}), \qquad [2]$$

will relate the orientations between two faces in adjacent cells, where the products are taken over edges on paths between the two faces. This also means that the lattice vectors obtained by summing along edges, $\mathbf{l}_{1(2)} \equiv \sum_{1(2)} \mathbf{r}_{(i,j)}$ can only be defined in the first cell, and undergo rotations given by the lattice rotation matrices in other cells. Hence, in contrast with a conventional crystal whose cells are translations of one another along lattice vectors, the origami sheet is *screw-periodic*: cells are related by screw motions consisting of translations and rotations (see Fig. 1b).

Any valid configuration, satisfying Eqn. 1, must define unique relative orientations and positions of cells regardless of the path between them. Considering a loop between cells, such as the four colored cells in Fig. 1b, leads to the inter-cell position and compatibility conditions,

$$\mathbf{S}_1\mathbf{S}_2 = \mathbf{S}_2\mathbf{S}_1, \qquad [3]$$

$$\mathbf{l}_1 + \mathbf{S}_1\mathbf{l}_2 = \mathbf{l}_2 + \mathbf{S}_2\mathbf{l}_1. \qquad [4]$$

These conditions imply there is a unique rotation axis (except for flat sheets, and a few pathological cases that we will not consider), denoted by $\hat{s}$, and a unique radius of curvature so that the sheet generically approximates a cylinder as shown in Fig 1b (see SI Appendix 2 for a characterization of this cylinder) (34). The familiar case of spatially periodic origami then emerges as the special limit in which the lattice rotations, $\mathbf{S}_{1,2}$, become identity matrices while arbitrary configurations with non-zero Gaussian curvature cannot be rigidly folded from periodic angles. Given the position of each vertex in the origin cell, denoted by $\mathbf{r}_i$, we can compute the position of an arbitrary vertex by summation of all edge vectors traveled along to reach it

$$\mathbf{r}_i(\mathbf{n}) = \sum_{n'=0}^{n_1-1} \mathbf{S}_1^{n'}\mathbf{l}_1 + \mathbf{S}_1^{n_2} \sum_{n'=0}^{n_1-1} \mathbf{S}_2^{n'}\mathbf{l}_2 + \mathbf{S}_1^{n_1}\mathbf{S}_2^{n_2}\mathbf{r}_i, \qquad [5]$$

where the order of summation can be interchanged by orientation and position compatibility, Eqns. 3 and 4 (see SI Appendix 3 for an evaluation of the summations over lattice rotations).

Those compatibility conditions allow a prediction for the dimension of the space of cylindrical configurations of a triangulated origami. Consider a potential configuration specified by the positions of each vertex, the two lattice vectors, and the two lattice rotation matrices. A rigidly folded configuration of the triangulation must preserve the length of each edge and satisfy position and orientation compatibility. Euler's polyhedron formula states that the numbers of faces, edges and vertices must satisfy $N_v - N_e + N_f = \chi$, where the Euler

characteristic χ vanishes for a doubly periodic surface. Every face in a triangulation has three edges, each shared with exactly one face so that $N_e = (3/2)N_f$, thereby implying $N_e = 3N_v$. In this way, each three-dimensional vertex position is accounted for via three edge constraints. Additionally, there are twelve numbers that specify the lattice vectors and lattice rotation matrices. The compatibility conditions supply four constraints: that the direction of the axis of the second rotation is shared by that of the first, and that two components of the position vectors in Eq. 4 are equal (the third direction, along the shared axis, is guaranteed to be equal). This leaves an eight-dimensional space of configurations of the sheet, six of which are simply rigid rotations and translations, leaving a *two-dimensional* space of rigidly foldable deformations. This was observed by Tachi (34), who advanced a similar counting argument. We will see these deformations emerge explicitly by considering higher-order rigidity conditions, which also reveal subtle branching behavior around the flat state. Helical, cylindrical tubes have the two additional constraints that the ratios of lattice rotation angles, $2\pi\theta_1/\theta_2$, and on-axis components of the lattice vectors $l_1^{\hat{s}}/l_2^{\hat{s}}$ are rational to ensure closure, which generically renders the tubes rigid. Allowing the tube to close without vertices connecting relieves the second of these conditions and permits motion by slip with a single degree of freedom (48).

3. Linear folding motions from global symmetries via vertex duality

A. Relationship between folding angles and vertex displacements. The cylindrical symmetries of origami correspond to rigid body modes which are paired with force-bearing modes at the Maxwell point (49, 50). These force-bearing modes, however, are identical to infinitesimal changes in the fold angles, ϕ_{ij}, which satisfy the vertex condition, Eqn. 1, to first-order (33, 45, 46). Here, we combine this mechanical duality with the mechanical criticality of Maxwell origami to show rigid body modes generate linear folding motions independent of the sector angles.

Consider infinitesimal changes (zero modes) $\phi_{(i,j)}$ to the fold angles $\rho_{(i,j)}$. The linearization of Eqn. 1, as shown in (51) and recapitulated in SI Appendix 4, is

$$\sum_{(i,j)} \phi_{(i,j)}(\mathbf{n})\hat{r}_{(i,j)}(\mathbf{n}) = \mathbf{0}, \qquad [6]$$

where the edges rotate $\hat{r}_{(i,j)}(\mathbf{n}) = \mathbf{S}_1^{n_1}\mathbf{S}_2^{n_2}\hat{r}_{(i,j)}$ between cells by Eqn. 5. The infinitesimal rotation of a face (i,j,k) may be described by an "angular velocity" vector $\boldsymbol{\omega}_{(i,j,k)}$ such that any vector $\mathbf{v}$ on the face, including edge vectors, undergoes a rotation $\mathbf{v} \to \mathbf{v} + \boldsymbol{\omega}_{(i,j,k)} \times \mathbf{v}$ as shown in Fig. 1c. Two faces sharing an edge must then induce the same rotation upon it, leading to a relation between adjacent angular velocities and the folding angle of the edge between them:

$$\boldsymbol{\omega}_{(i,j,l)} - \boldsymbol{\omega}_{(i,j,k)} = \phi_{(i,j)}\hat{r}_{(i,j)} \qquad [7]$$

These then accumulate such that the angular velocity of one face relative to a fixed face is

$$\boldsymbol{\omega}_{(i,j,k)}(\mathbf{n}) = \sum_{(i',j')} \phi_{(i',j')}(\mathbf{n}')\hat{r}_{(i',j')}(\mathbf{n}'), \qquad [8]$$

where the sum is over all edges crossed on a path between the faces. Similarly, the displacement of a vertex on a distant face is given by the sum of all vertex displacements along the path from a fixed vertex, which are in turn determined by rotating the bond vectors via their respective angular velocities:

$$\mathbf{u}_k(\mathbf{n}) = \sum_{(i',j')} \boldsymbol{\omega}_{(i',j',k')}(\mathbf{n}') \times \mathbf{r}_{(i',j')}(\mathbf{n}'). \qquad [9]$$

This summation is explicitly evaluated for both the spatially periodic and screw periodic cases in SI Appendix 7.

Having described how vertex positions may be generated via arbitrary folding motions, we may complete the identification by a map from the vertex positions of an isometry back to the folding motions. The procedure is to take two edge vectors along a face, $\mathbf{r}_{(i,j)}, \mathbf{r}_{(k,j)}$ and the normal vector $\mathbf{N}_{(i,j,k)} = \mathbf{r}_{(i,j)} \times \mathbf{r}_{(k,j)}$ and to consider the changes implied by the vertex displacements to the two vectors $\mathbf{u}_{(i,j)}, \mathbf{u}_{(k,j)}$ and to the normal vector $\delta\mathbf{N}_{(i,j,k)} = \mathbf{r}_{(i,j)} \times \mathbf{u}_{(k,j)} + \mathbf{u}_{(i,j)} \times \mathbf{r}_{(k,j)}$ This yields the matrix equation

$$\boldsymbol{\omega}^{\times}_{(i,j,k)} \begin{pmatrix} \mathbf{r}_{(i,j)} & \mathbf{r}_{(k,j)} & \mathbf{N}_{(i,j,k)} \end{pmatrix} = \begin{pmatrix} \mathbf{u}_{(i,j)} & \mathbf{u}_{(k,j)} & \delta\mathbf{N}_{(i,j,k)} \end{pmatrix} \qquad [10]$$

which may be inverted to obtain $\boldsymbol{\omega}^{\times}_{(i,j,k)}$, the cross-product matrix whose elements give the angular velocity of the face. From these angular velocities Eqn. 7 may be used to obtain the changes to the folding angles.

B. Duality between folding motions and tensions. The linear folding constraint, Eqn. 6, takes the familiar form of tensions $t_{(i,j)}$ along edges $\hat{r}_{(i,j)}$ that yield no net force called *states of self stress* (33, 45, 46). This hidden symmetry between static and kinematic modes has particular significance for periodic sheets, for which it implies symmetrically distributed edge modes, as we discuss later. The concatenation of Eqn. 6 at each vertex within the origin cell yields the equilibrium matrix, $\mathbf{Q}$, that maps tensions to the net force on each vertex. Importantly, the static-kinematic duality reveals that the transpose of the equilibrium matrix is the compatibility matrix, $\mathbf{C} = \mathbf{Q}^T$, that maps vertex displacements to bond extensions (50). This leads, via the rank-nullity theorem of linear algebra, to the celebrated Maxwell-Calladine index theorem relating the number of zero energy vertex displacements, N_{zm}, to the number of states of self stress, N_{ss}, within the origin cell (49, 50)

$$N_{zm} - N_{ss} = 3N_v - N_e. \qquad [11]$$

We are now able to combine the criticality of triangulated origami, which ensures the right-hand side vanishes, with the duality between states of self stress and folding modes to use spatial symmetries to guarantee the existence of folding modes, some of which have already been observed. Spatially periodic sheets have three translational modes, implying three states of self stress and three folding motions, as observed in triangulations of the Miura-ori and eggbox crease patterns (23–27). In contrast, cylindrical sheets have only two rigid-body modes: translations along and rotations about the axis, implying the two linear motions that lead to the two-dimensional space of configurations. In either case, fusing two triangular faces together to create a quadrilateral face eliminates a degree of freedom, reducing the space of rigid configurations. More generally, folding motions are possible in origami above the

Maxwell point due to symmetries, e.g. the Miura-ori, that render constraints degenerate as has been observed in spring networks (52).

4. Nonlinear constraints lead to branching between cylindrical configurations

In this section, we describe the full set of nonlinear rigid folds of the origami sheets. Spatially periodic states have three linear modes and we employ second-order rigidity conditions to identify how they extend to the nonlinear branches. As we show, the necessary requirement that the linear modes generate a cylindrical surface is sufficient for a second-order folding motion to exist. The surface of modes in configuration space (parametrized by the fold angles) is generally two-dimensional, with two two-dimensional branches connected at the flat state. In contrast, in developable sheets up to 2^{N_v+1} branches can meet at the flattened state, with every sheet investigated showing pairs of branches distinguished by whether a vertex pops upward or downward, as previously observed in origami sheets with one-dimensional configuration spaces (19).

While first-order compatibility is sufficient to ensure a cylindrical configuration folds into another cylindrical configuration (see SI Appendix 7), the lattice rotation axes spontaneously chosen when folding from a spatially periodic state are not necessarily coaxial. We can see this by noting the expansion of orientation compatibility, Eqn. 3, about the flat state, where the lattice rotations are identity matrices, is trivially satisfied to first-order. Instead, the leading order contribution is given

$$\delta\mathbf{S}_1\delta\mathbf{S}_2 = \delta\mathbf{S}_2\delta\mathbf{S}_1, \qquad [12]$$

where the $\delta\mathbf{S}_{1,2}$ are skew-symmetric generators of rotation whose components are given by the inter-cell angular velocity $\sum_{1,2}\phi_{(i,j)}\hat{r}_{(i,j)}$ computed from Eqn. 8 (see SI Appendix 7). From position compatibility, Eqn. 4, we have at first-order $\delta\mathbf{S}_1\mathbf{l}_2 = \delta\mathbf{S}_2\mathbf{l}_1$, implying these rotations lie in the plane of the origami sheet defined by $\mathbf{l}_1 \times \mathbf{l}_2$ so that Eqn. 12 has only a single nonzero entry. Taking linear combinations of the linear folding motions, $\phi_{(i,j)} = \sum_\alpha \lambda_\alpha \phi^\alpha_{(i,j)}$, this becomes a quadratic expression in the real coefficients, λ_α, which will generically admit two distinct families of solutions, $\lambda^\pm_\alpha$, that correspond to upwards or downwards folded cylinders. We note real solutions to Eqn. 12 do not always exist, as is the case for the triangulated Miura-ori, which prevents its out-of-plane linear motions from extending nonlinearly (23), however we find real solutions generically exist for our Maxwell origami sheets without any fine-tuning.

That the linear folding motions yield a cylindrical configuration turns out to be a sufficient condition for the existence of second-order folding motions, $\delta\phi_{(i,j)}$, which satisfy the vertex constraint, Eqn. 1, to second-order. This second-order vertex condition consists of a linear term in $\delta\phi_{(i,j)}\hat{r}_{(i,j)}$ and a quadratic sum of pairwise products of $\phi_{(i,j)}\hat{r}_{(i,j)}$ over each edge connected to a particular vertex i (see SI Appendix 5 for an expansion of Eqn. 1)

$$\sum_{(i,j)} \delta\phi_{(i,j)}\hat{r}_{(i,j)} + \sum_{(i,j)} \phi_{(i,j)} \left(\sum_{\substack{(i,k)\\k<j}} \phi_{(i,k)}\hat{r}_{(i,k)} \right) \times \hat{r}_{(i,j)} = \mathbf{0}, \qquad [13]$$

where $k < j$ denotes the interior sum is taken over successive indices clockwise from j up to the starting edge. The interior sum of the second term gives, by Eqn. 8, the angular velocity of a face relative to the starting face at vertex i so that the cross product gives the rotation of edge $\hat{r}_{(i,j)}$ with the first edge of the sum held fixed. By the first-order condition, Eqn. 6, we can add any constant angular velocity, $\boldsymbol{\omega}_i$, to this sum since the exterior sum $\boldsymbol{\omega}_i \sum \phi_{(i,j)} \times \hat{r}_{(i,j)}$ vanishes, allowing us to rewrite Eqn. 13 as

$$\sum_{(i,j)} \delta\phi_{(i,j)}\hat{r}_{(i,j)} + \sum_{(i,j)} \phi_{(i,j)}\delta\hat{r}_{(i,j)} = \mathbf{0}, \qquad [14]$$

where $\delta\hat{r}_{(i,j)}$ depends on the coefficients, λ_α, used to construct the linear folding motion and are themselves linear in the $\phi_{(i,j)}$. This means when we concatenate Eqn. 14 at each vertex, the first term is the action of the equilibrium matrix on the second-order folding motions, $\mathbf{Q}\delta\boldsymbol{\phi}$, while the second term is the action of the *change* in the equilibrium matrix due to a linear folding motion on the linear folding motions, $\delta\mathbf{Q}\boldsymbol{\phi}$, where we use bold to denote the vector of fold angle changes $\boldsymbol{\phi} = (\ldots, \phi_{(i,j)}, \ldots)$.

Since we have already restricted our linear folding motions to those which yield cylindrical configurations, the compatibility matrix of the linearly deformed state, $\mathbf{C}' = \mathbf{C} + \delta\mathbf{C}$, must admit zero modes, $\mathbf{u}'$, corresponding to translations and rotations about the uniquely defined axis. These are paired with states of self stress, $\mathbf{t}'$, that lie in the nullspace of the new equilibrium matrix, $\mathbf{Q}' = \mathbf{Q} + \delta\mathbf{Q}$, via mechanical criticality which, by the mechanical duality, are isomorphic to linear folding motions $\boldsymbol{\phi}'$. Such new linear folding motions can generically be written as a combination of the linear folding motions in the original configuration, $\boldsymbol{\phi}$, along with a correction, $\delta\boldsymbol{\phi}$, that satisfies Eqn. 14 after dropping the higher-order term $\delta\mathbf{Q}\delta\boldsymbol{\phi}$. Hence, the existence of the second-order folding motions of Eqn. 14 is guaranteed so long as the first-order motions generate a cylindrical surface. As shown explicitly in SI Appendix 6, this result can also be derived via the mechanical duality, which reveals a connection between rigid translations and rotations.

Finally, let us consider developable origami sheets in the flat state which admit extra linear folding motions (the generalization to origami sheets with both developable and non-developable vertices is straightforward). This can be seen by noting Eqn. 6 only furnishes two constraints per vertex when all edges lie in a plane. These additional folding motions are paired with zero modes that correspond to vertices popping up or down out of the plane (19, 20). Generally, this yields an extra $N_v - 1$ linear folding motions for developable origami in the flat state (the rigid-body translation in the direction normal to the sheet can be written as a linear combination of the N_v additional modes arising from developability) which do not all extend to rigid folding motions. The N_v seemingly missing constraints are provided by the quadratic term in Eqn. 13. Since every edge lies in the same plane, this yields a single constraint per vertex. Moreover, this term is in the left nullspace of the equilibrium matrix so no $\delta\phi_{(i,j)}$ are needed to satisfy Eqn. 1 to second-order. We generalize our definition of sector angles so that $\alpha_{(i,j,k)}$ is the angle between edges $\mathbf{r}_{(i,j)}$ and $\mathbf{r}_{(i,k)}$ which do not necessarily share a face but are coplanar. Eqn. 13 then simplifies to the scalar equation for a developable vertex i

$$\sum_{(i,j)} \sum_{\substack{(i,k) \\ k>j}} \phi_{(i,j)} \phi_{(i,k)} \sin(\alpha_{(i,j,k)}) = 0. \qquad [15]$$

By taking linear combinations of our folding motions, we can find simultaneous solutions to the N_v second-order constraints. While there are up to 2^{N_v+1} complex roots by Bézout's theorem (19, 53), we are only interested in the real-valued solutions whose existence depends on the crease geometry. Since a developable sheet has reflection symmetry through the plane of the sheet, these roots come in pairs which fold upwards or downwards into indistinguishable cylinders. In other words, for N branches there are only $N/2$ unique branches which cannot be obtained by rotations of the remaining $N/2$ branches.

5. Numerical investigation of nonlinear folding

We now show corrections exist at all orders by numerically evolving periodic origami sheets. We begin with a spatially periodic, non-developable origami sheet composed of six triangular faces and a single quadrilateral face in each cell (this unit cell with four vertices is the simplest pattern with no trivial creases), as labeled by the star in Fig. 2, and rigidly fold along its one-dimensional branches. Following, we add a crease across the diagonal of the quadrilateral face, allowing the sheet to explore its two-dimensional space of rigidly foldable configurations embedded in the N_e-dimensional configuration space. Alternatively we may obtain a one-dimensional path through the two-dimensional configuration space by locking the fold angle on any edge whether or not the adjacent faces form a polygon. To visualize this surface, we project into a three-dimensional space spanned by strains of the lattice vectors. We use the three independent components, $(\epsilon_{11}, \epsilon_{22}, \epsilon_{12})$, of the in-plane deformation tensor determined via changes to the lengths and angle between the lattice vectors as described in SI Appendix 9.

In Fig. 2, we show the branched one-dimensional paths and the two-dimensional surfaces corresponding to configurations of the origami sheet along with a spatial configuration of the sheet on each branch (see Supplementary Movie 1 for evolution along this surface). The branches are colored according to the configuration's radius of curvature at each state, where the sign is chosen to designate whether the sheet folded upwards or downwards. In SI Appendix 8, we discuss how the spatial embedding and curvature direction of these configurations is obtained from the fold angles. These trajectories close when allowing for self-intersection of the origami sheet (some fold angles pass through $\pm\pi$ at which point adjacent faces intersect), as shown in the inset of Fig. 2 which, although unphysical for origami, may have consequences in the behavior of equivalent systems such as spin origami (54). Although the two-dimensional surfaces close, we only show a closed one-dimensional path as otherwise features are obscured by spurious self-intersections due to different configurations with the same in-plane strains despite having distinct fold angles.

We next construct a developable origami sheet with a single quadrilateral face in the flat state. Our arbitrarily chosen crease pattern yields six real solutions to Eqn. 15, indicating six branches from the flat state. We show three of these branches in Fig. 3 (each branch has a beginning and end which join in the flat state), all with positive radius of curvature (see Supplementary Movie 2 for evolution along this surface). The remaining three branches have the exact same in-plane strains with equal and opposite radii of curvature. The number of branches is a property of the crease geometry and we do not address a method for controlling the number of branches here. In fact, even identical triangulations with different faces fused into a quadrilateral substantially effects which strains and curvatures (geometry) occur in addition to the number of branches (topology). For developable origami, the lattice vectors are maximal in the flattened state so any folding results in $\epsilon_{11}, \epsilon_{22} < 0$, while shearing allows for either positive or negative values of ϵ_{12}.

6. Pairing of spatially varying modes at opposite wavenumbers

In the previous sections we considered the pairing of rigid-body modes and deformations with the same fold angle changes in every cell. Here, we generalize the mechanical duality to spatially varying modes to investigate the topological mechanics of Maxwell origami whose connections to quantum mechanical systems such as topological insulators (41), nodal semimetals (42), dissipative systems (55) and spin origami (54, 56–58) are discussed in SI Appendix 10. These spatially varying zero modes are normal modes of the system (with frequency zero) and so, due to Bloch's theorem, must take the forms

$$\mathbf{u}_i(\mathbf{n}) = \mathbf{u}_i z_1^{n_1} z_2^{n_2}, \quad \phi_{(i,j)}(\mathbf{n}) = \phi_{(i,j)} z_1^{n_1} z_2^{n_2}, \qquad [16]$$

for Bloch factors $z_i = e^{iq_i}$ with wavenumbers q_i which may be complex for general boundary conditions. The mapping from vertex displacements to folding motions in Eqn. 9 extends naturally to the spatially varying modes, which inherit the same dependence on wavenumber so that, by the mechanical duality of origami, there is a mapping between zero modes and states of self stress at finite wavenumber $N_{zm}(\mathbf{q}) = N_{ss}(\mathbf{q})$.

The finite wavenumber static-kinematic duality relates the equilibrium matrix to the transpose of the compatibility matrix at the *opposite* wavenumber, $\mathbf{Q}(\mathbf{q}) = \mathbf{C}^T(-\mathbf{q})$, modifying the Maxwell-Calladine index theorem of Eqn. 11 to (37, 38)

$$N_{zm}(\mathbf{q}) - N_{ss}(-\mathbf{q}) = 3N_v - N_e, \qquad [17]$$

which pairs zero modes at $\mathbf{q}$ with self stresses at $-\mathbf{q}$ (this sign difference, crucial for our argument, has been omitted previously). This leads to the intriguing scenario, identified by Kane and Lubensky (41), in which a zero mode may be exponentially localized to one edge (at some complex $\mathbf{q}$) with a state of self stress at the opposite edge (at $-\mathbf{q}$), creating an excess or deficit of zero modes on an edge or interface beyond that predicted by local coordination number, which is known as topological polarization. The localization of these modes can be characterized by an inverse decay rate $\kappa_{1(2)} = -\mathrm{Im}(q_{1(2)})$, where, e.g. $\kappa_2 < 0 (\kappa_2 > 0)$ indicates the mode is exponentially localized on the bottom (top) edge as shown in Fig 4a-b.

Since these states of self stress can themselves be mapped onto zero modes via the duality discussed above for triangulated surfaces, whenever there is a zero mode at $\mathbf{q}$ there must also be one at $-\mathbf{q}$, as shown by the pairing of inverse decay rates in Fig. 4a. This means while it is always possible to impose a periodic distortion on a surface and, by the fundamental theorem of algebra, find a mode that exponentially decays into the bulk, the hidden symmetry guarantees that there is a corresponding mode on the opposing side. This shows

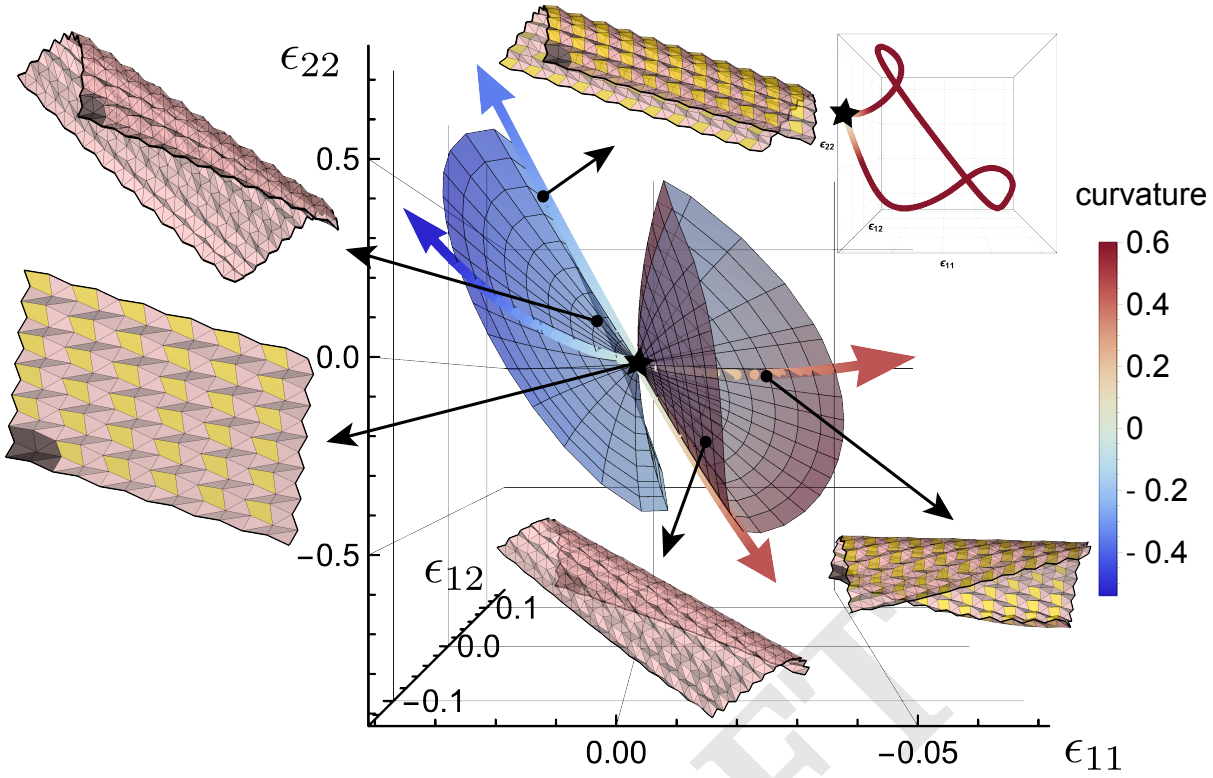

Fig. 2. The 2-dimensional surface of rigidly foldable configurations for a nondevelopable triangulated origami sheet projected from its N_e-dimensional configuration space to the 3-dimensional strain space (see SI Appendices 8 and 9) where coloring indicates the signed radius of curvature at each point. Arrows point from a point in this space to the corresponding reconstructed sheet with cell $\mathbf{n} = (0, 0)$ colored in gray. Some origami sheets have two triangular faces fused into a rigid quadrilateral marked in yellow, restricting the folding motions from the full 2D surfaces to one-dimensional paths marked with curved, multi-colored arrows. The yellow quadrilateral indicates a polygonal face which restricts the sheet to 1-dimensional trajectories. The distinct branches correspond to origami sheets which fold upwards or downwards from the flat state. The boxed inset shows two one-dimensional folding trajectories as they close into a single loop over high strains.

polarization can never occur in Maxwell origami as observed by Chen et al. (47). In fact the same work found Maxwell kirigami, composed of equal numbers of quadrilateral faces and holes, to topologically polarize is reconciled by a generalized version of the mechanical duality which pairs folding motions of the original structure with the self stresses of a distinct structure obtained by replacing all faces with a hole and vice versa (59), thereby breaking the hidden symmetry.

Interestingly, this characteristic of Maxwell origami, while eliminating the Kane Lubensky invariant, generates a new topological property. The determinant of the compatibility matrix becomes a Laurent polynomial in the Bloch factors, $\det \mathbf{C}(\mathbf{q}) = \sum_{m,n} c_{mn} z_1^m z_2^n$, where the highest-order of m and n is given by the total number of edges passing from the unit cell to the $\mathbf{n} = (1, 0)$ and $\mathbf{n} = (0, 1)$ cells respectively and c_{mn} are real coefficients determined by the crease geometry. This determinant vanishes at wavenumbers admitting zero modes, and previously it has been shown in 2D Maxwell lattices (42) that the real and imaginary parts of the compatibility matrix generically vanish at zero-dimensional points within the 2D Brillouin Zone. In the present case, the existence of zero modes at equal and opposite wavenumbers implies this determinant must be purely real so there instead appear 1D lines of zero modes, as shown in Fig. 4a, corresponding to the lines of magnetic waves observed in a quantum analog of origami sheets (54). Furthermore, the sign of the real compatibility matrix serves as a topological invariant which changes only when crossing such a line of zero modes as shown in Fig. 4c.

It is not clear how these linear modes extend into nonlinear deformations. By mechanical criticality, a triangulated sheet with open boundaries must have modes due to the missing constraints at the edges. In general, though, the existence of such finite-wavenumber modes is guaranteed only by continuous symmetries that are broken as the mode is extended nonlinearly. In particular finite-wavenumber modes will induce sinusoidally varying amounts of Gaussian curvature through the sheet in contrast to the uniform folding motions that extend nonlinearly.

7. Conclusion

We have considered the rigid foldability of periodically triangulated origami with generic crease patterns and constructed a counting argument via Maxwell origami's combined mechanical duality and mechanical criticality. That argument shows translational and rotational rigid-body modes ensure the existence of folding motions that extend nonlinearly to yield two-dimensional spaces of rigidly foldable origami configurations which branch from the spatially periodic configuration. Furthermore, we showed this allows construction of crease patterns with a single degree of freedom simply by adding a single quadrilateral face to the unit cell. We leave for future work the refinement of our counting argument to address how discrete

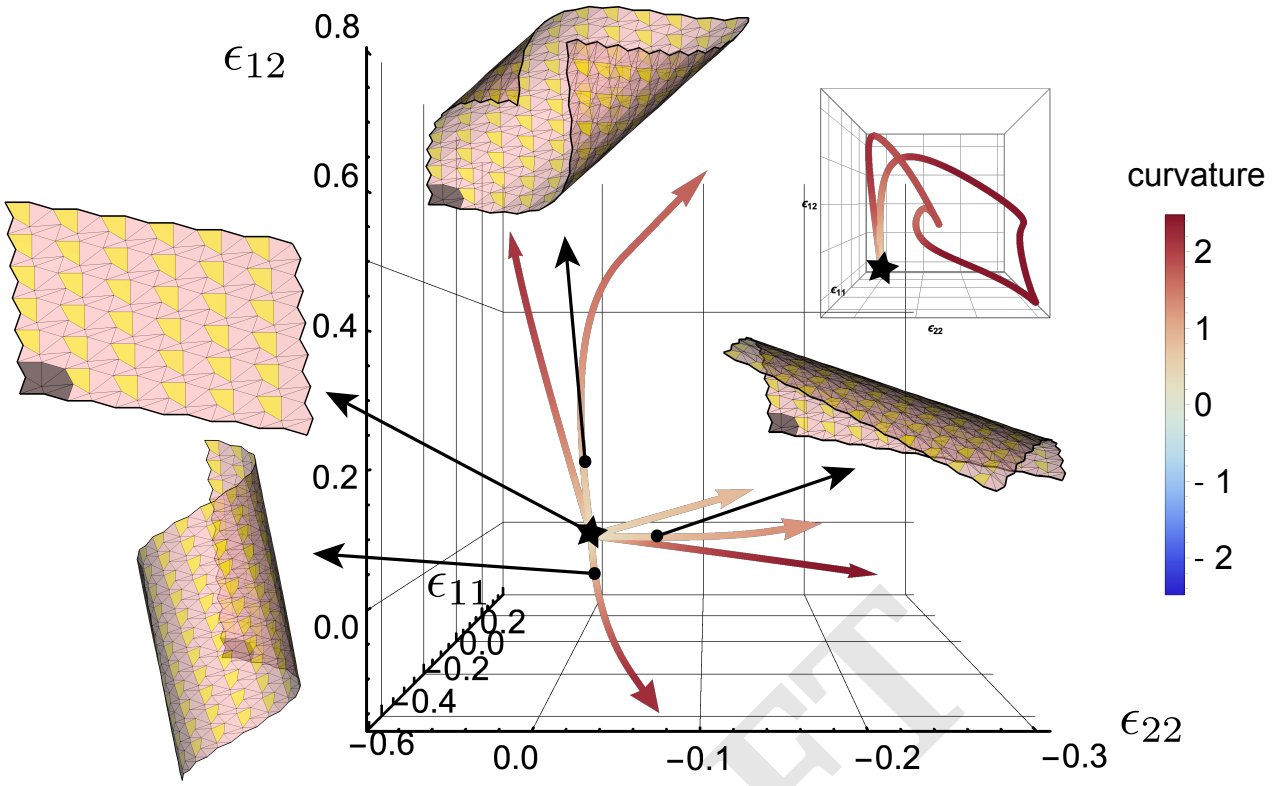

Fig. 3. The 1-dimensional lines of rigidly foldable configurations for a developable origami sheet with one quadrilateral face per unit cell projected from its N_e-dimensional configuration space to the 3-dimensional strain space (see SI Appendices 8 and 9) where coloring indicates the signed radius of curvature at each point where the flattened configuration is labeled by a star. Arrows point from a branch in this space to the corresponding reconstructed sheet with cell $\mathbf{n} = (0, 0)$ colored in gray and the insets show a full one-dimensional orbit through the configuration space when constraining the fold angle on an edge. Our randomly generated crease pattern admits 6 solutions to Eqn. 15 and hence has 3 branches with strictly positive radii of curvature. There are 3 additional branches with identical strains and the oppositely signed curvatures.

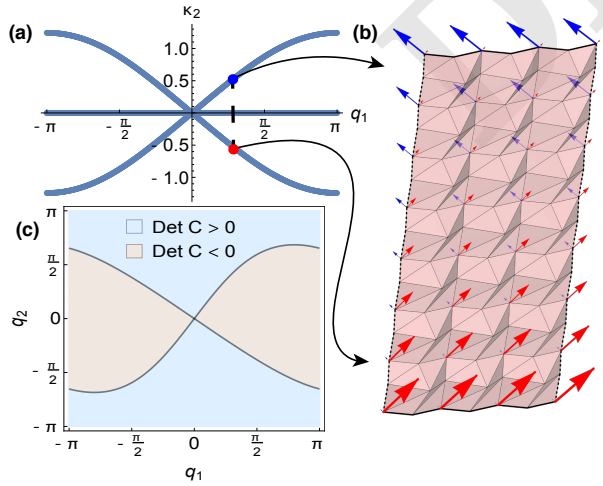

Fig. 4. (a) The signed inverse decay lengths, κ_2, along the $\mathbf{l}_2$ direction for zero modes at particular, real assignments of q_1. The line along the origin corresponds to bulk zero modes that have zero inverse decay length everywhere. (b) The spatially periodic origami sheet shown in (a) with blue (red) arrow indicating zero mode vertex displacements on one vertex per cell (additional arrows omitted for visual clarity) that grow towards the top (bottom). (c) The determinant of the compatibility matrix for the origami sheet in panel (b) across the Brillouin zone.

symmetries can permit non-triangulated patterns, such as the Miura-ori, to rigidly fold.

Finally, we have extended our counting argument to spatially varying modes, revealing that edge modes necessarily appear in pairs on opposite sides, explaining the lack of polarization previously observed (47). Our analysis reveals the existence of one-dimensional lines of bulk zero modes in Maxwell origami, as opposed to zero-dimensional points, that could be used to reconfigure the origami sheet by introducing an expanded unit cell. This also identifies a new topological invariant based on this hidden symmetry between folding motions and states of self stress that may lead to additional topological properties (60). The generality of our results is unique in that it depends only on the coordination of the crease pattern rather than the specific geometry which may aid in the design of foldable materials in hard-to-control, microscopic environments.

Materials and Methods

We use Mathematica 12 to evolve our rigid origami. Each step of the trajectory first finds the tangent plane in the configuration space by computing the nullspace of the linear vertex condition. We then project the previous direction into this basis to minimize the change in our tangent vector at each step of the trajectory. Then, using Mathematica's *FindMinimum* function, we evolve our origami sheet in this direction satisfying the vertex condition to numerical precision 10^{-16} using the BFGS QuasiNewton method.

ACKNOWLEDGMENTS. B.G.C. thanks funding from NSF Award No. PHY-1554887. C.S. thanks funding from NSF DMR-1822638. J.M. thanks funding from the Georgia Institute of Technology President's Fellowship and the STAMI Graduate Student Fellowship.

1. Elliot Hawkes, B An, Nadia M Benbernou, H Tanaka, Sangbae Kim, ED Demaine, D Rus, and Robert J Wood. Programmable matter by folding. *Proceedings of the National Academy of Sciences*, 107(28):12441–12445, 2010.
2. Michael T Tolley, Samuel M Felton, Shuhei Miyashita, Daniel Aukes, Daniela Rus, and Robert J Wood. Self-folding origami: shape memory composites activated by uniform heating. *Smart Materials and Structures*, 23(9):094006, 2014.
3. Marc Z Miskin, Kyle J Dorsey, Baris Bircan, Yimo Han, David A Muller, Paul L McEuen, and Itai Cohen. Graphene-based bimorphs for micron-sized, autonomous origami machines. *Proceedings of the National Academy of Sciences*, 115(3):466–470, 2018.
4. Noy Bassik, George M Stern, and David H Gracias. Microassembly based on hands free origami with bidirectional curvature. *Applied physics letters*, 95(9):091901, 2009.
5. Ying Liu, Julie K Boyles, Jan Genzer, and Michael D Dickey. Self-folding of polymer sheets using local light absorption. *Soft matter*, 8(6):1764–1769, 2012.
6. Jun-Hee Na, Arthur A Evans, Jinhye Bae, Maria C Chiappelli, Christian D Santangelo, Robert J Lang, Thomas C Hull, and Ryan C Hayward. Programming reversibly self-folding origami with micropatterned photo-crosslinkable polymer trilayers. *Advanced Materials*, 27 (1):79–85, 2015.
7. Koryo Miura. Method of packaging and deployment of large membranes in space. *Title The Institute of Space and Astronautical Science Report*, 618:1, 1985.
8. Kaori Kuribayashi, Koichi Tsuchiya, Zhong You, Dacian Tomus, Minoru Umemoto, Takahiro Ito, and Masahiro Sasaki. Self-deployable origami stent grafts as a biomedical application of ni-rich tini shape memory alloy foil. *Materials Science and Engineering: A*, 419(1-2):131–137, 2006.
9. Rui Tang, Hai Huang, Hongen Tu, Hanshuang Liang, Mengbing Liang, Zeming Song, Yong Xu, Hanqing Jiang, and Hongyu Yu. Origami-enabled deformable silicon solar cells. *Applied Physics Letters*, 104(8):083501, 2014.
10. Zeming Song, Teng Ma, Rui Tang, Qian Cheng, Xu Wang, Deepakshyam Krishnaraju, Rahul Panat, Candace K Chan, Hongyu Yu, and Hanqing Jiang. Origami lithium-ion batteries. *Nature communications*, 5:3140, 2014.
11. Jiayao Ma and Zhong You. The origami crash box. *Origami*, 5:277–290, 2011.
12. Xueli Liu, Shun Yao, Benjamin S Cook, Manos M Tentzeris, and Stavros V Georgakopoulos. An origami reconfigurable axial-mode bifilar helical antenna. *IEEE Transactions on Antennas and Propagation*, 63(12):5897–5903, 2015.
13. Lakshminarayanan Mahadevan and Sergio Rica. Self-organized origami. *Science*, 307 (5716):1740–1740, 2005.
14. Hugo Akitaya, Erik D Demaine, Takashi Horiyama, Thomas C Hull, Jason S Ku, and Tomohiro Tachi. Rigid foldability is np-hard. *arXiv preprint arXiv:1812.01160*, 2018.
15. belcastro Sarah-Marie and Thomas C Hull. Modelling the folding of paper into three dimensions using affine transformations. *Linear Algebra and its applications*, 348(1-3):273–282, 2002.
16. Bin Liu, Jesse L Silverberg, Arthur A Evans, Christian D Santangelo, Robert J Lang, Thomas C Hull, and Itai Cohen. Topological kinematics of origami metamaterials. *Nature Physics*, 14(8):811, 2018.
17. Scott Waitukaitis, Rémi Menaut, Bryan Gin-ge Chen, and Martin van Hecke. Origami multistability: From single vertices to metasheets. *Physical review letters*, 114(5):055503, 2015.
18. Menachem Stern, Matthew B Pinson, and Arvind Murugan. The complexity of folding self-folding origami. *Physical Review X*, 7(4):041070, 2017.
19. Bryan Gin-ge Chen and Christian D Santangelo. Branches of triangulated origami near the unfolded state. *Physical Review X*, 8(1):011034, 2018.
20. M Berry, ME Lee-Trimble, and CD Santangelo. Topological transitions in the configuration space of non-euclidean origami. *arXiv preprint arXiv:1910.01008*, 2019.
21. Jesse L Silverberg, Arthur A Evans, Lauren McLeod, Ryan C Hayward, Thomas Hull, Christian D Santangelo, and Itai Cohen. Using origami design principles to fold reprogrammable mechanical metamaterials. *science*, 345(6197):647–650, 2014.
22. Jesse L Silverberg, Jun-Hee Na, Arthur A Evans, Bin Liu, Thomas C Hull, Christian D Santangelo, Robert J Lang, Ryan C Hayward, and Itai Cohen. Origami structures with a critical transition to bistability arising from hidden degrees of freedom. *Nature materials*, 14(4):389, 2015.
23. Zhiyan Y Wei, Zengcai V Guo, Levi Dudte, Haiyi Y Liang, and L Mahadevan. Geometric mechanics of periodic pleated origami. *Physical review letters*, 110(21):215501, 2013.
24. Mark Schenk and Simon D Guest. Geometry of miura-folded metamaterials. *Proceedings of the National Academy of Sciences*, 110(9):3276–3281, 2013.
25. Cheng Lv, Deepakshyam Krishnaraju, Goran Konjevod, Hongyu Yu, and Hanqing Jiang. Origami based mechanical metamaterials. *Scientific reports*, 4:5979, 2014.
26. Hussein Nassar, Arthur Lebée, and Laurent Monasse. Curvature, metric and parametrization of origami tessellations: theory and application to the eggbox pattern. *Proceedings of the Royal Society A: Mathematical, Physical and Engineering Sciences*, 473(2197):20160705, 2017.
27. Phanisri P Pratapa, Ke Liu, and Glaucio H Paulino. Geometric mechanics of origami patterns exhibiting poisson's ratio switch by breaking mountain and valley assignment. *Physical review letters*, 122(15):155501, 2019.
28. Evgueni T Filipov, Tomohiro Tachi, and Glaucio H Paulino. Origami tubes assembled into stiff, yet reconfigurable structures and metamaterials. *Proceedings of the National Academy of Sciences*, 112(40):12321–12326, 2015.
29. Arthur A Evans, Jesse L Silverberg, and Christian D Santangelo. Lattice mechanics of origami tessellations. *Physical Review E*, 92(1):013205, 2015.
30. Scott Waitukaitis and Martin van Hecke. Origami building blocks: Generic and special four-vertices. *Physical Review E*, 93(2):023003, 2016.
31. Peter Dieleman, Niek Vasmel, Scott Waitukaitis, and Martin van Hecke. Jigsaw puzzle design of pluripotent origami. *Nature Physics*, pages 1–6, 2019.
32. Matthew B Pinson, Menachem Stern, Alexandra Carruthers Ferrero, Thomas A Witten, Elizabeth Chen, and Arvind Murugan. Self-folding origami at any energy scale. *Nature communications*, 8:15477, 2017.
33. Herman Gluck. Almost all simply connected closed surfaces are rigid. In *Geometric topology*, pages 225–239. Springer, 1975.
34. Tomohiro Tachi. Rigid folding of periodic origami tessellations. *Origami*, 6:97–108, 2015.
35. Mark Schenk and Simon D Guest. Origami folding: A structural engineering approach. In *Origami 5: Fifth International Meeting of Origami Science, Mathematics, and Education*, pages 291–304. CRC Press, Boca Raton, FL, 2011.
36. ET Filipov, K Liu, T Tachi, M Schenk, and GH Paulino. Bar and hinge models for scalable analysis of origami. *International Journal of Solids and Structures*, 124:26–45, 2017.
37. TC Lubensky, CL Kane, Xiaoming Mao, Anton Souslov, and Kai Sun. Phonons and elasticity in critically coordinated lattices. *Reports on Progress in Physics*, 78(7):073901, 2015.
38. Xiaoming Mao and Tom C Lubensky. Maxwell lattices and topological mechanics. *Annual Review of Condensed Matter Physics*, 9:413–433, 2018.
39. SD Guest and JW Hutchinson. On the determinacy of repetitive structures. *Journal of the Mechanics and Physics of Solids*, 51(3):383–391, 2003.
40. Ciprian S Borcea and Ileana Streinu. Periodic frameworks and flexibility. *Proceedings of the Royal Society A: Mathematical, Physical and Engineering Sciences*, 466(2121):2633–2649, 2010.
41. CL Kane and TC Lubensky. Topological boundary modes in isostatic lattices. *Nature Physics*, 10(1):39, 2014.
42. D Zeb Rocklin, Bryan Gin-ge Chen, Martin Falk, Vincenzo Vitelli, and TC Lubensky. Mechanical weyl modes in topological maxwell lattices. *Physical review letters*, 116(13):135503, 2016.
43. D Zeb Rocklin. Directional mechanical response in the bulk of topological metamaterials. *New Journal of Physics*, 19(6):065004, 2017.
44. D Zeb Rocklin, Shangnan Zhou, Kai Sun, and Xiaoming Mao. Transformable topological mechanical metamaterials. *Nature communications*, 8(1):1–9, 2017.
45. Henry Crapo and Walter Whiteley. Statics of frameworks and motions of panel structures: a projective geometric introduction. *Structural Topology, 1982, núm. 6*, 1982.
46. Tomohiro Tachi. Design of infinitesimally and finitely flexible origami based on reciprocal figures. *J. Geom. Graph*, 16(2):223–234, 2012.
47. Bryan Gin-ge Chen, Bin Liu, Arthur A Evans, Jayson Paulose, Itai Cohen, Vincenzo Vitelli, and CD Santangelo. Topological mechanics of origami and kirigami. *Physical review letters*, 116(13):135501, 2016.
48. Fan Feng, Paul Plucinsky, and Richard D. James. Helical miura origami. *Phys. Rev. E*, 101: 033002, Mar 2020. . URL https://link.aps.org/doi/10.1103/PhysRevE.101.033002.
49. J Clerk Maxwell. L. on the calculation of the equilibrium and stiffness of frames. *The London, Edinburgh, and Dublin Philosophical Magazine and Journal of Science*, 27(182):294–299, 1864.
50. CR Calladine. Buckminster fuller's "tensegrity" structures and clerk maxwell's rules for the construction of stiff frames. *International journal of solids and structures*, 14(2):161–172, 1978.
51. Tomohiro Tachi. Simulation of rigid origami. *Origami*, 4:175–187, 2009.
52. SD Guest and PW Fowler. Symmetry-extended counting rules for periodic frameworks. *Philosophical Transactions of the Royal Society A: Mathematical, Physical and Engineering Sciences*, 372(2008):20120029, 2014.
53. Joe Harris. *Algebraic geometry: a first course*, volume 133. Springer Science & Business Media, 2013.
54. Krishanu Roychowdhury, D Zeb Rocklin, and Michael J Lawler. Topology and geometry of spin origami. *Physical review letters*, 121(17):177201, 2018.
55. Zongping Gong, Yuto Ashida, Kohei Kawabata, Kazuaki Takasan, Sho Higashikawa, and Masahito Ueda. Topological phases of non-hermitian systems. *Physical Review X*, 8(3): 031079, 2018.
56. EF Shender, VB Cherepanov, PCW Holdsworth, and AJ Berlinsky. Kagomé antiferromagnet with defects: Satisfaction, frustration, and spin folding in a random spin system. *Physical review letters*, 70(24):3812, 1993.
57. P Chandra, P Coleman, and I Ritchey. The anisotropic kagome antiferromagnet: a topological spin glass? *Journal de Physique I*, 3(2):591–610, 1993.
58. I Ritchey, Premala Chandra, and Piers Coleman. Spin folding in the two-dimensional heisenberg kagomé antiferromagnet. *Physical Review B*, 47(22):15342, 1993.
59. Wendy Finbow, Elissa Ross, and Walter Whiteley. The rigidity of spherical frameworks: swapping blocks and holes. *SIAM Journal on Discrete Mathematics*, 26(1):280–304, 2012.
60. Krishanu Roychowdhury and Michael J Lawler. Classification of magnetic frustration and metamaterials from topology. *Physical Review B*, 98(9):094432, 2018.